Modelling the primary damage in Fe and W: Influence of the short range interactions on the cascade properties: Part 1 – Energy transfer

Charlotte Becquart, Andrée de Backer, Pär Olsson, Christophe Domain

Version of Record: https://www.sciencedirect.com/science/article/pii/S0022311521000398
Manuscript_abaf996fae902d94159f282fcd2a0c3e

Modelling the primary damage in Fe and W: influence of the short range interactions on the cascade properties: part 1 – energy transfer.

Charlotte S. Becquart[1,2], Andrée De Backer[1,2,3], Pär Olsson[4], Christophe Domain[5,2]

[1] Univ. Lille, CNRS, INRAE, Centrale Lille, UMR 8207 - UMET - Unité Matériaux et Transformations, F-59000 Lille, France

[2] EM2VM, Joint laboratory Study and Modeling of the Microstructure for Ageing of Materials

[3] CCFE, Culham Centre for Fusion Energy, Abingdon, Oxon, United Kingdom

[4] KTH Royal Institute of Technology, Nuclear Engineering, Roslagstullsbacken 21, SE-10691 Stockholm, Sweden

[5] EDF-R&D, Département Matériaux et Mécanique des Composants, Les Renardières, F-77250 Moret sur Loing, France

Corresponding author: Charlotte S. Becquart (charlotte.becquart@univ-lille.fr)

Abstract

The primary damage in metallic alloys, i.e. the point defect distribution resulting from the interaction between an energetic particle and a metallic matrix has been investigated for more than 60 years using atomistic simulations. The defect distribution produced in cascades is sensitive to the equilibrium part of the potential as well as its hardened part. An analysis based on large statistics of molecular dynamics simulations and comparison with different embedded atom method potentials in Fe and W allows to rationalize the potential behavior. Correlations between static non-equilibrium properties (quasi static drag (QSD)), threshold displacement energies (TDE), replacement collision sequences (RCS) along the ⟨110⟩ direction have been revealed. Along this direction, the lower the TDE, the lower the QSD and the more energy is transmitted along the ⟨110⟩ direction during the RCS, i.e. the softest potentials are the ones for which the most energy is transmitted from the PKA to the first head-on atom in the direction of the RCS sequence.

Key words

Radiation damage, Primary damage, Displacement cascades, Primary knock on atom, Metallic alloys, Empirical potentials, Threshold Displacement Energies.

Highlights

-Strong correlation between mean threshold displacement energy for ⟨110⟩ direction; the quasi static drag curve along ⟨110⟩, replacement collision sequences (RCS) along ⟨110⟩ and the number of defects created during displacement cascades in two bcc metals Fe and W. The properties of the potentials along this direction should thus be carefully assessed during the hardening of the potentials.

-Soft potentials produce longer RCS but the energy at which the RCS length decreases is lower for soft potentials.

-The length of replacement collision sequences (RCS) in dense ⟨111⟩ directions has a maximum value because of the energy transfer regime.

Graphical abstract

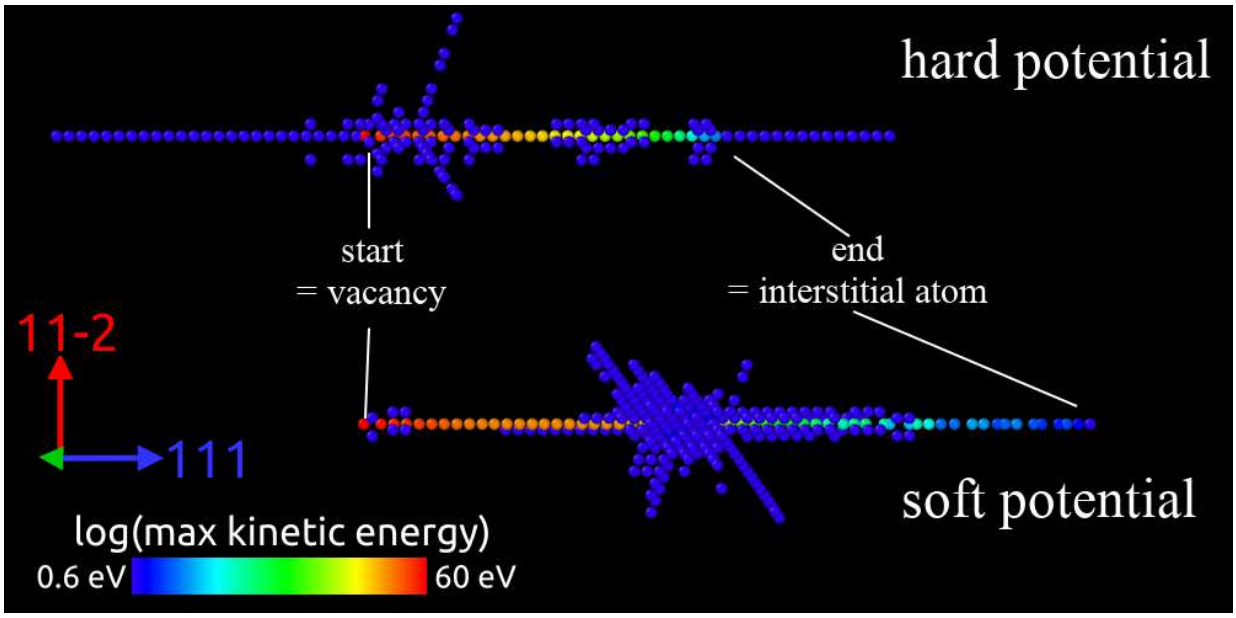

Introduction

The study of radiation damage has a long history. Damage is initiated through the interaction by a highly energetic particle with atoms in a material, starting a series of energetic Primary Knock-on Atom (PKA) collisions. Significant efforts are devoted to identify the mechanisms of damage and to predict the evolution, over time, of the microstructure and mechanical properties of materials under irradiation. Since these elementary mechanisms cannot yet be directly observed by experimental techniques due to their very short life times (a few picoseconds), and small spatial extent (between a few to several hundred Ångströms), the most appropriate approach is modelling, using techniques from the atomic scale, such as the binary collision approximation (BCA) and molecular dynamics (MD) which are perfectly suited to simulate primary damage formation.

The cohesive model, which describes the interactions between atoms, is the keystone of these simulations and it is necessary to characterize it well before starting any simulation. For MD simulations, the interaction potentials can be established using electronic structure calculations. However, these “ab initio” methods are very expensive in terms of computation time, and their introduction into an atomistic scale simulation code is only possible for systems of small sizes, especially when magnetism has to be taken into account. In order to simulate systems containing more particles, one usually resorts to approximate solutions (empirical or semi-empirical) of these potentials, adjusted to physical properties of the material studied. These empirical interatomic potentials (EIP) are usually mathematical functions allowing to calculate the potential energy of the system. They are generally intended for the study of phenomena for which the material remains in a situation close to equilibrium and are adjusted accordingly to some of its equilibrium and near-equilibrium properties.

During displacement cascades and in particular for highly energetic PKAs, the distance between the atoms can momentarily become much less than the distance between first neighboring atoms at equilibrium. It is therefore necessary to extend ("harden") equilibrium potentials for small distances. Historically, for the very short range, the Ziegler-Biersack-Littmark [1] (ZBL) screened Coulomb interaction is used and spliced to the equilibrium potential using various interpolation schemes. The distances at which the interpolation scheme starts and ends is usually chosen arbitrarily by the person hardening the potential and no standard procedure exists. The only guideline in the hardening procedure was to make sure that the EIP predicted threshold displacement energies (TDE) close to the experimental values. This was proven not to be enough in [2] where three EIPs for Fe, predicting very similar TDEs, were shown to predict very different cascades and damage distributions. Furthermore, [3] found that the [0-200 eV] range of the potential is decisive for the production of focusing chains, i.e. replacement collision sequences (RCS) and focusons in Fe. More recently, one W potential that was spliced to the ZBL using two different interpolation schemes lead to very different displacement cascades [4] and thus to very different damage. With the increasing power of super computers, help to solve this issue can be found in quantum mechanics first principles

calculations as proposed around the same time in [5] and [6]. Density functional theory (DFT) can be used on large enough supercells to simulate RCS focusing chains and even obtain TDE (at 0 K) [5] and can thus be used to compare with the predictions of empirical potentials.
In this work, we compare the quality of a large number of EIPs for fundamental energy transfer quantities for tungsten and iron. For this purpose we have undertaken to compare the prediction of the potentials for point defect related properties, threshold displacement energies, replacement collision sequences and focusons, as well as the evolution of the total energy of the system when one atom is moved step by step along a specific direction (this is referred to as quasi static drag (QSD) [5], with the results of DFT using two kinds of potentials: the minimal set regular projector augmented-wave *(*PAW) which, for tungsten considers 6s and 5d electrons as valence electrons and the semi-core PAW which also includes the 5p electrons explicitly. The minimal set regular PAW is referred to as DFT_{sd}, whereas the semi-core PAW is referred to as DFT_{psd}. Using these potentials, a very large database of displacement cascades has been created and analyzed, looking for correlations between the resulting primary damage and the potential properties.

After a short description of the potentials assessed in this work, we analyze and compare their static and dynamic properties as well as their prediction of TDE along 4 directions: ⟨100⟩, ⟨110⟩, ⟨111⟩ and ⟨135⟩.
In the companion paper to this one [7], we will analyze the damage predictions for displacement cascades generated by cascade energy up to 100 keV and underline the correlations between the potential properties and their predictions and compare the damage prediction in Fe and W.

I. Empirical potentials used and DFT calculations

1) Description of the EIP investigated

For W, we have tested four modified versions of the potential originally derived by Finnis and Sinclair [8]: one version modified by Mason et al. [9], that will be referred to as MN, one version modified by Juslin et al. [10], referred to as JW, one version modified by Derlet et al. [11] and hardened by Björkas et al. [12], referred to as DD and one derived by Ackland and Thetford [13] and hardened by Zhong et al. [14] referred to as AT. A new potential derived by Marinica et al. [15] and hardened in two different ways (softer and harder) by Sand [4] will be referred to as MS-s and MS-h. The potential derived by Mason et al. has also been hardened in two different ways also and the two versions will be referred to as MN-s and MN-h.

For Fe, the potentials investigated will be referred to as MA10A for the MO7 potential initially published in [16], MEND10 for the potential derived by Ackland et al. [17] and CO21013, CO21620 and CO30912 for potentials newly derived by Marinica et al. [18] and hardened in this work. The hardening procedure is described in the supplementary material. The choice of the positions of the points where the different functions meet (the splicing points) was done by trial and error in order to be as close as possible to the quasi static drag (QSD) curves obtained by DFT (Figure 1).

Table 1: origins of the different potentials used

Name	Authors of the original potential	Hardened potential
W EIP		
DD	Derlet, Nguyen Manh, Dudarev [11]	Bjorkas, Nordlund, Dudarev [12]
JW	Juslin and Wirth [10]	Juslin and Wirth [10]
MN-s	Mason, Becquart and Nguyen Manh [9]	Mason [9]
MN-h	Mason, Becquart and Nguyen Manh [9]	Mason [9]
MS-s	Marinica, Ventelon, Gilbert, Proville, Dudarev, Marian, Bencteux, Willaime [15]	Sand, Dequeker, Becquart, Domain, Nordlund [4]
MS-h	Marinica, Ventelon, Gilber, Proville, Dudarev, Marian, Bencteux, Willaime [15]	Sand, Dequeker, Becquart, Domain, Nordlund [4]
AT	Ackland and Thetford [13]	Zhong, Nordlund, Ghaly, and Averback [14]
Fe EIP		
MA10A	Malerba, Marinica, Anento, … [16]	This work (see supplementary)
MEND10	Ackland, Mendelev, Srolovitz, Han and Barashev. [17]	Ackland [17]
CO21013N	Alexander, Marinica and Proville [18]	This work (see supplementary)
CO21013D	Alexander, Marinica and Proville [18]	This work (see supplementary)
CO21620	Alexander, Marinica and Proville [18]	This work (see supplementary)
CO30912	Alexander, Marinica and Proville [18]	This work (see supplementary)

2) Description of the DFT calculations

In this work, all the ab initio calculations have been done using the Vienna Ab initio Simulation Package VASP [19] [20]. They were performed within density functional theory (DFT), using pseudopotentials from the VASP library that were generated within the projector augmented wave (PAW) approach [21] [22]. The calculations were spin polarized for bcc Fe and the exchange-correlation functional is described by the generalized gradient approximation (GGA) of Perdew et al. [23], with the Vosko-Wilk-Nusair (VWN) interpolation of the correlation energy [24]. Periodic boundary conditions and the supercell approach were used for all calculations. The Brillouin zone was sampled using the Monkhorst-Pack scheme [25]. The plane wave energies were cut off at 250 eV for Fe and 230 eV for W. For the quasi static drag calculations, the cut off were 300 eV for Fe and 250 eV for W. The calculations were done using the minimal set regular PAW, which, for tungsten considers 6s and 5d electrons and for Fe 4s and 3d electrons as valence electrons and the semi-core PAW which also includes the 5p

and 3p electrons explicitly. The minimal set regular PAW is referred to as DFT_{sd}, whereas the semi-core PAW is referred to as DFT_{psd}.

II. Methods used to characterize and compare the EIP

1) QSD: quasi static drag

In order to better understand the difference observed between the DFT and the empirical potentials we have performed quasi-static drag (QSD) simulations of the initial stage in the defect creation process. For this purpose, an atom is dragged step-wise along a displacement vector and the energy response of the system is recorded as proposed in [5] [4]. We find that this method allows to probe different regions of the interaction models if it is done along different crystallographic directions as shown in **Table 2** and to analyze how the different interaction models respond to local anisotropic compression. It is furthermore very easy to calculate for any cohesive model (DFT or empirical potential), and can be readily used to compare cohesive models. QSD is very similar to the dimer in the lattice proposed in [6]. The QSD was recorded along four directions ⟨100⟩, ⟨110⟩, ⟨111⟩ and ⟨135⟩. All the QSD calculations (for both DFT and the EP) were done in 686-atom supercells and 1 k-point. We found after different trials that the results were converged for this supercell size.

Figure 1 compares the QSD for the DFT calculations as well as using the ZBL formula, for the ⟨100⟩, ⟨110⟩, ⟨111⟩ and ⟨135⟩ directions. During its travel, regardless of the direction, the dragged atom passes close to atoms situated more or less close to the drag direction. For instance, along ⟨100⟩, the drag atom goes through a window of four atoms, the four atoms situated at the corners of the cube. These neighbor atoms it passes by, will be referred to as the "barrier atoms" (**Figure 2**). Note that along ⟨111⟩, the drag atom goes through two "windows" of three barrier atoms each. The first window is situated 0.29 lattice units (l.u.) from the drag atom initial position, the second one is at 0.58 l.u. on the ⟨111⟩ row. The first atom that the dragged atom will encounter in the drag direction, i.e., the next atom, on the row, will be referred to as the head on atom. Along ⟨110⟩ and ⟨135⟩ directions, the barrier atoms are quite close to the dragged atom as shown in **Table 2** and a bump in the QSD curve can be seen (**Figure 1).** This bump characterizes the interactions of the dragged atom with its barrier atoms. Depending on the potential, the bump is more or less pronounced and for the DFT_{sd} calculations they are quite small. Along the ⟨100⟩ and ⟨111⟩ direction no such bumps are visible and the difference between the two sets of DFT calculations is mostly the distance at which the dragged atom starts "feeling" the effect of the head on atom. For the minimum set DFT calculations, DFT_{sd}, the dragged atom can move closer to the head on atom (i.e. the distance to its initial position is larger) before the energy of the system starts increasing significantly. These curves indicate that, as expected, DFT_{sd} is always much softer than DFT_{psd} and is too soft. Furthermore, the ZBL formula for both metals is very close to the DFT semi core results of W whatever the direction below 50 eV. Above that energy, the DFT_{psd} for W remains still very close to ZBL for the same metal, whereas ZBL for Fe is higher than DFT_{sd} until a value between 100 and 160 eV where the two curves cross (except for ⟨135⟩).

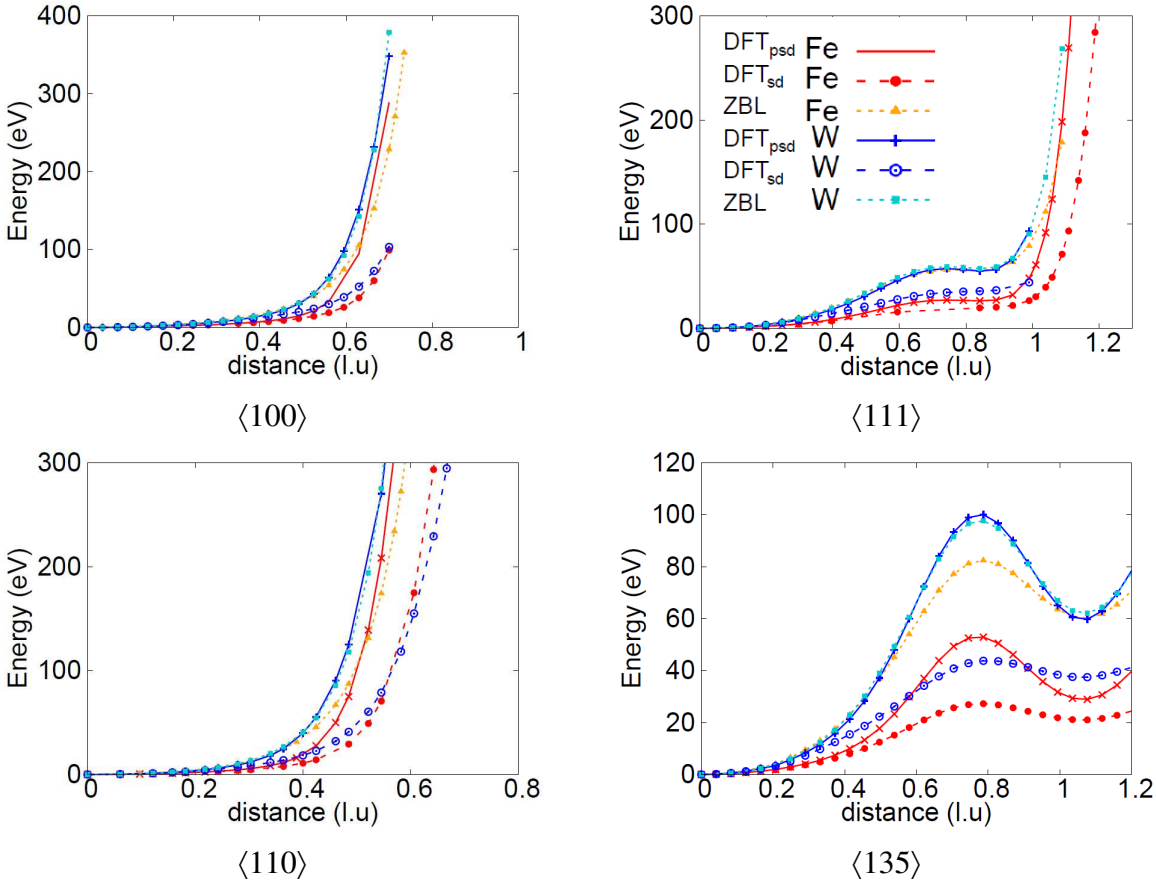

Figure 1: QSD along the four directions for Fe and W with the two DFT approaches and the ZBL formula. The caption is similar for all directions.

Table 2: Characteristics of the QSD trajectories. The barrier atoms are the neighbor atoms of the row.The head on atom is the next atom in the row. Along ⟨100⟩, the drag atom goes through a window of four atoms (the four atoms situated at the corners of the cube). Along ⟨111⟩, the drag atom goes through two windows of three barrier atoms each. The first window of such barrier atom is situated 0.29 l.u. from the drag atom. The different distances are represented on **Figure 2.**

Direction	Corr. letter on Fig 2	⟨100⟩	⟨110⟩	⟨111⟩ 1st window	⟨111⟩ 2nd window	⟨135⟩
Closest distance between the drag atom and the barrier atoms i.e. when the drag atom is at the center of the barrier atom window (l.u.)	a	0.707	0.5	0.816	0.816	0.414
Distance between window center and drag atom initial position	b	0.5	0.707	0.29	0.58	0.774

(l.u.)						
Distance between window center and head on atom (l.u.)	c	0.5	0.707	0.58	0.29	2.18
Number of barrier atoms at the closest distance from the drag atom		4	2	3	3	1

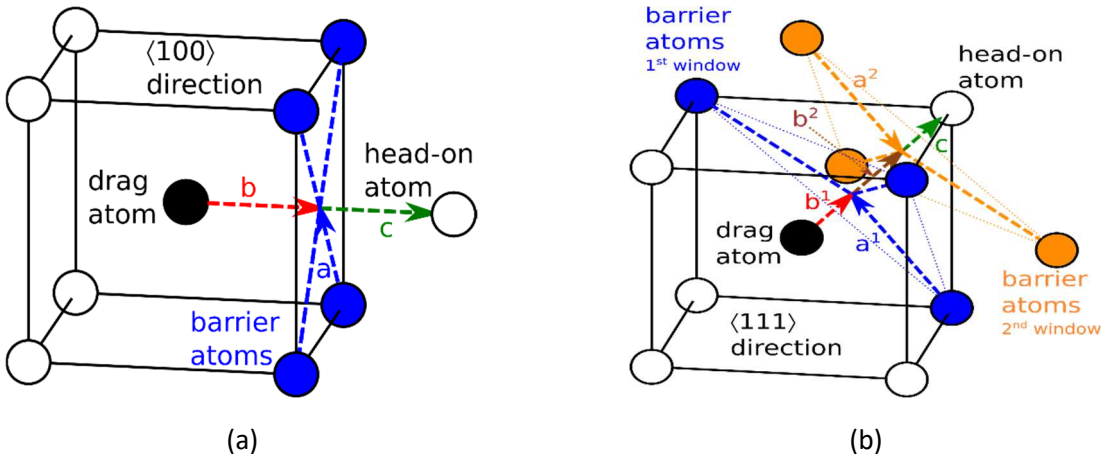

Figure 2: Explanation of the different distances of interest on QSD trajectories. (a) along ⟨100⟩ (b) along ⟨111⟩

2) Linear collision sequences: RCS and focusons

Replacement collision and focuson sequences are linear collision sequences (LCS) playing an important role in the development of displacement cascades and the spatial extent of the primary damage. They are means to transport over long distances part of the energy transferred to the PKA. RCS contributes to matter transport whereas focusons transport energy only [26]. Focusing chain simulations provide thus information on how much and how kinetic energy is transferred and lost in atomic collisions. Linear collision sequences are simulated by giving to one atom, an impulse in a high-symmetry direction. One then monitors the kinetic energy loss per collision. The energy has to be high enough to create many collisions (typically well above the TDE). We showed, using BCA and MD simulations in Fe, that the [0-200 eV] energy range of the potential is the one governing the RCS production [3] and that the shorter the potential range, the larger the energy dissipated by RCS at the expense of energy dissipated by focusons, and the more Frenkel pairs formed [26].

The linear collision sequences along ⟨111⟩ have been studied in large boxes with orientation $\langle 1\bar{1}0\rangle$, $\langle 11\bar{2}\rangle$, ⟨111⟩ in order to have a long box in the LCS direction, for 3 ps using MD at 0 K in the microcanonical (NVE) ensemble. The sides of the box were adjusted to prevent the sequence to interact with itself and were as large as ($8 \times \sqrt{6}$ l.u.) × ($14 \times \sqrt{2}$ l.u.) × ($100\ \sqrt{3}$ l.u.) for W and ($8 \times \sqrt{6}$ l.u.) × ($14 \times \sqrt{2}$ l.u.) × ($90\ \sqrt{3}$ l.u.) for Fe.

Figure 3 shows an example of the variation with time of the kinetic energy in a 100 eV linear collision sequence along ⟨111⟩ at 0 K using "ab initio" MD and DFT_{sd} for W. The figure displays a series of black curves, each one containing one major and a couple of minor peaks (not shown on the figure). Each black curve corresponds to one atom in the sequence. The first atom (which will be referred to as the PKA for the sake of clarity, even though, as discussed in [27], in "real life" the PKA energy is partitioned into the damage energy due to elastic processes and energy losses due to electronic stopping) has received a kinetic energy of 100 eV along the ⟨111⟩ direction. Its kinetic energy decreases while it exits from its potential well and interacts with the barrier atoms and with the first head on atom. The next peak corresponds to the temporal dependence of the kinetic energy of the PKA's first neighbor in the direction of the replacement sequences (the first head on atom), the third peak to that of the PKA's second neighbor (or the second atom first neighbor along the replacement collision direction), and so on. The energy loss per collision, along the collision sequence, appears to be constant (except for the first collision which requires additional energy to create a FP) at the beginning of the sequence, as shown by the fact that the maximum kinetic energy for neighbor atoms (the height of each peaks) decreases in a quasi linear manner. The transmitted energy gradually decreases from one collision to the next one and very little energy is transferred to the barrier atoms (the kinetic energy of the barrier atoms is not shown on this figure for the sake of clarity).

In the ⟨111⟩ direction, to reach another lattice site, the displaced atom has to move through two windows of three atoms situated at 0.29 ($\sqrt{3}/6$) and 0.58 ($\sqrt{3}/3$) lattice units, i.e. the displacement of which crosses the two brown lines on Figure 3. Atoms in the sequence that go through the two windows are permanently displaced, which is the case for atoms the index of which is lower than 92 in **Figure 4** whereas those that pass only through the first window (the index of which are higher than 92 in this case) will eventually move backwards to their original lattice site. When one or more atoms are permanently displaced, the sequence is thus bounded by a vacancy and a SIA (or a crowdion). Note that the vacancy is not always where the PKA was originally as it can move by several lattice sites along the sequence. **Figure 4** shows that the number of atoms permanently displaced is lower than the number of atoms moving in the sequence: the energy transfer sequence is longer than the replacement sequence. Thus, depending on the initial linear collision energy, the linear collision sequence can lead to energy transfer without matter transfer (focusons), i.e. the atoms are displaced during the sequence but they come back to their original position, or to energy and matter transfer through replacement sequences.

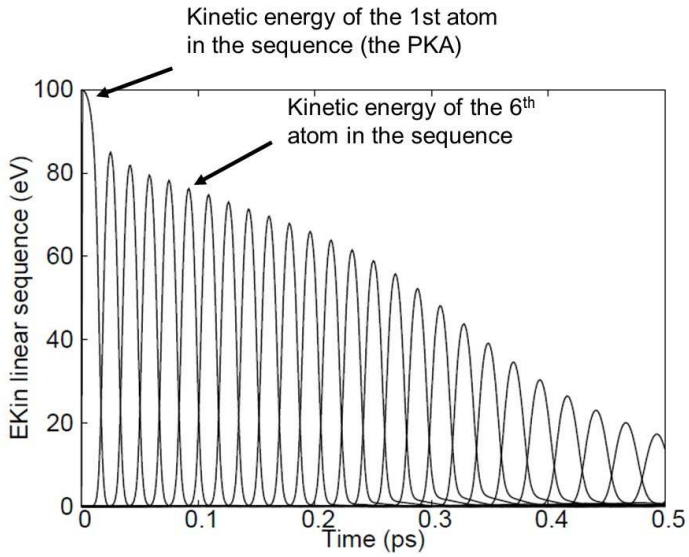

Figure 3: linear collision sequence initiated by a 100 eV PKA along ⟨111⟩ using DFT_{sd} for W. The supercell size contained 720 atoms, the time step was 1 fs and the number of k-points was 1. Each black curve corresponds to one atom in the sequence.

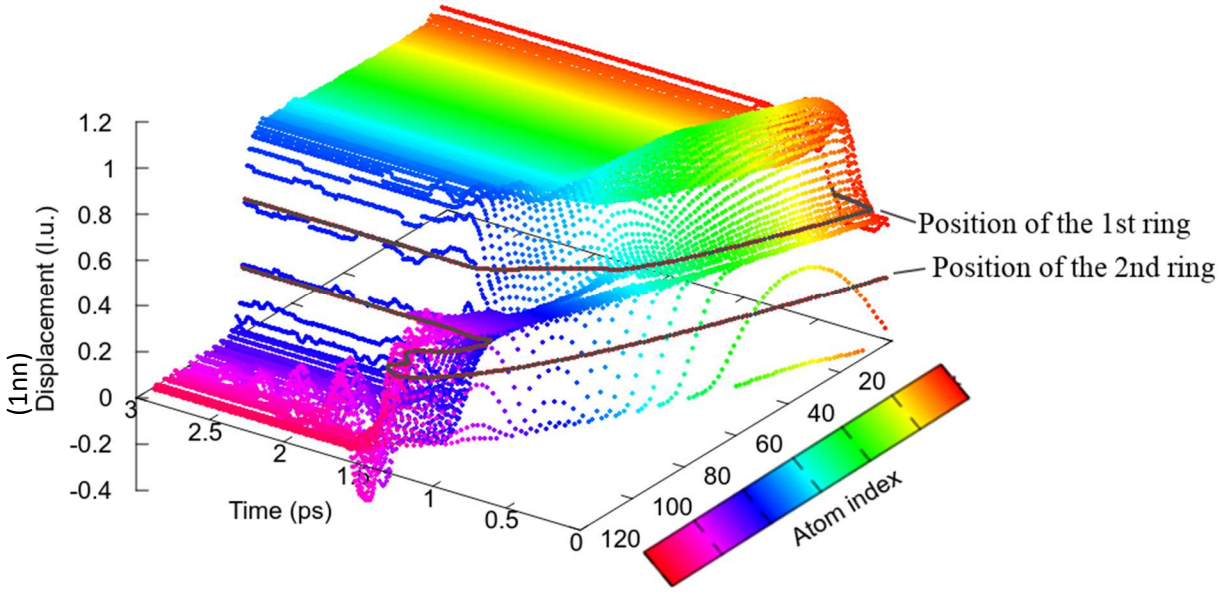

Figure 4: 3D plot showing for all the atoms in the ⟨111⟩ column (represented by their index in the column, the first atom in the column, i.e. the atom receiving the initial kinetic energy having index 1) their displacements (in units of the nearest neighbor distance (1nn)) as a function a time. The linear collision sequence has been initiated by atom 1 (the "PKA" atom) receiving a kinetic energy 70 eV along ⟨111⟩ modeled using the CO21620 potential (Fe). The displacements are represented using the vertical axis and the two brown lines indicate the position of the two windows of three barrier atoms (the two rings of atoms) the moving atoms pass through before reaching another lattice site.

3) TDE: threshold displacement energies

The TDE is defined as the minimum kinetic energy given to one atom in the lattice to create a stable FP. It depends on the material and on the orientation of the primary recoil. The average

TDE is the key materials parameter used to convert the absorbed irradiation dose, or damage energy [28] into the commonly used unit of displacements per atom (dpa). Even though we showed that having reasonable threshold displacement energies is not sufficient to guarantee that the hardened part of the potential is suited to model displacement cascade collision phase [2] [29], the TDE is still a critical potential parameter. We show, in the companion paper to this one, that unsurprisingly, a correlation can be found between the amount of point defects created and the TDE along the ⟨100⟩, ⟨110⟩, ⟨135⟩ directions, as found also in [30].

Experimental values of the TDE are available for a few elements and directions. In MD simulations of the literature, the TDE is the minimum amount of energy which must be given to one atom at the beginning of the simulation to have at least one stable FP at the end of the simulation. Because of the possible creation of metastable defects, different definitions can be used and a thorough discussion can be found in [31]. In this work, as in many cases, the TDE is estimated as the first energy value for which at least one vacancy remains in the system at the end of the simulation. To compare simulated TDEs with experimental ones require to take into account the spread of the experimental beam as proposed in [31]. Our purpose is to compare potentials and characterize them and not to compare directly with experiments. We thus chose to calculate the TDEs in tungsten and iron using all the interatomic potentials along 4 directions ⟨100⟩, ⟨110⟩, ⟨111⟩ and ⟨135⟩ according to the technique proposed by Setyawan et al. [32] using the MD code DYMOKA [33]. The simulations were launched in non cubic boxes 20 × 18 × 16 l.u.^{3} (11520 atoms) which were first thermalized for 6 ps at 10 K. For each direction, 200 simulations were done by systematically changing the initial lattice site from two thermalized simulations. As the energies of the collisions were low, we did not take account for electron-phonon coupling and electronic losses. The simulation proceeds as follows. We increase the energy by step of 5 eV until a Frenkel pair is created in the lattice. We then decrease the energy by step of 1 eV until we reach the PKA energy for which no FP is created. The TDE value we record is the energy of the last PKA in the decreasing energy sequence, for which one FP was created. The TDE values we consider for each potential is the mean of all the 200 values obtained using the procedure described previously. Because of the statistical nature of the threshold displacement energy [31], we may overestimate slightly the "real" value of the TDE, however, we feel that for our purpose which is to compare potentials, the method chosen here is appropriate enough.

III. Results

1) QSD

Figure 5 compares the QSD predicted by all the empirical potentials as well as by DFT. For W, the predictions from one potential to another differ by a much larger amount than for Fe. In particular, the two versions of MN and MS potentials are clearly different, helping us to investigate, in a more straightforward manner, the impact of the hardening of the potential on the radiation damage properties. Along the ⟨110⟩ and ⟨135⟩ directions, for the two soft potentials in W, MN-s and MS-s, the dragged atom hardly "feels" the barrier atoms as shown by the height of the bump. Furthermore, they have to come closer to the head on atom to start

“feeling” it as shown by the shift to the right of the sharp increase that is characteristic, in all QSD curves, when the screened Coulomb interaction starts to dominate.

For the Fe potentials, the behaviors are not so extreme, as the hardening of the potentials has been adjusted to be close to DFT, as shown in the supplementary material, however it can be observed that CO21620 is the softest potentials according to its QSD curves.

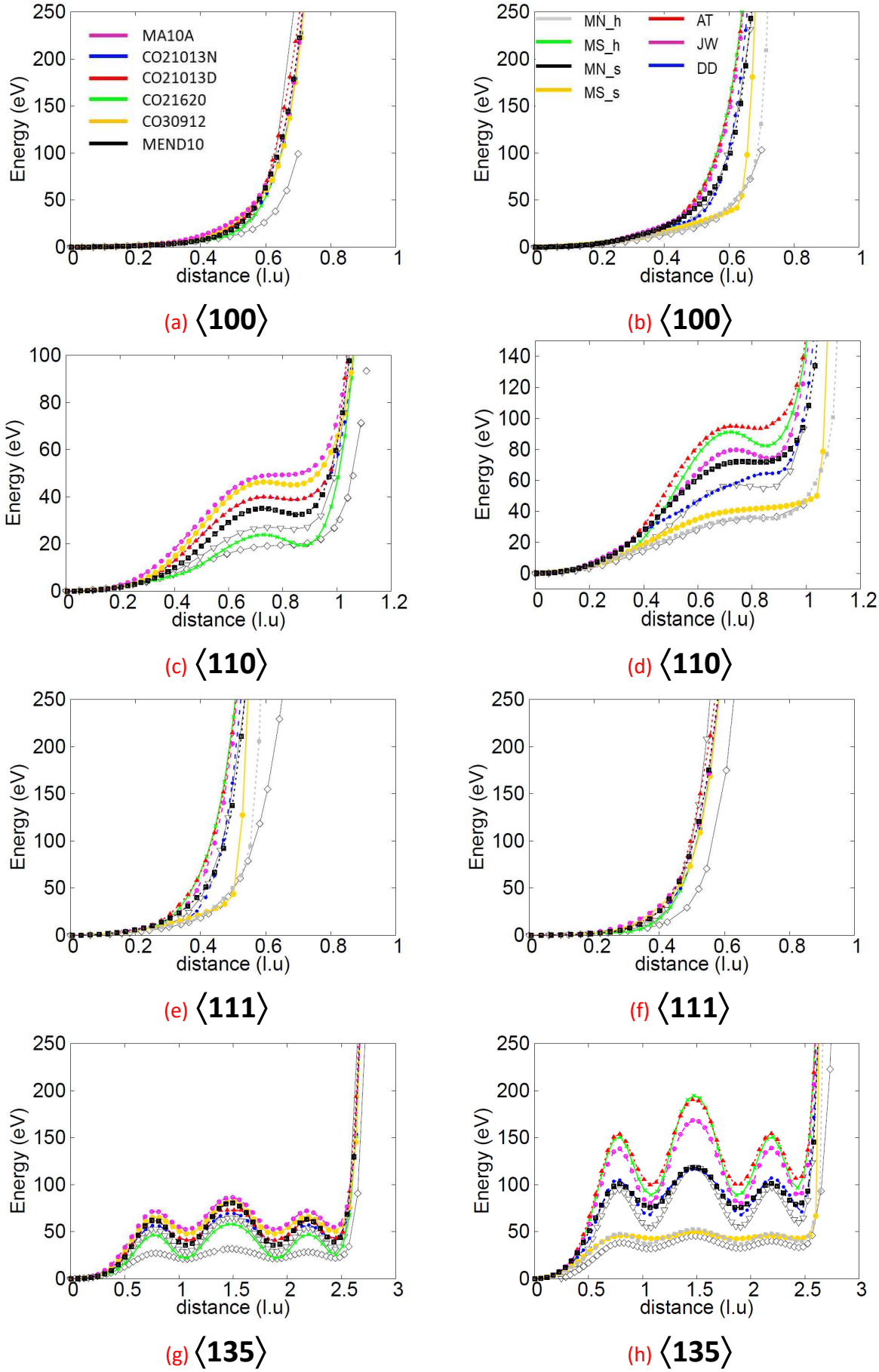

Figure 5: QSD for all the potentials and the four directions investigated in this work. From

top to bottom: (a) and (b):⟨100⟩, (c) and (d):⟨110⟩, (e) and (f): ⟨111⟩ and (g) and (h): ⟨135⟩. Left: Fe. Right: W.

2) Linear collision sequences

Linear collision sequence along ⟨110⟩

Figure 6 shows an example of the variation with time of the kinetic energy in linear collision sequences along ⟨110⟩ at 0 K for potentials in Fe and W. The black curves represent the kinetic energy of the atoms in the sequence (as described in **section II.2**); the red curves represent the kinetic energy of the barrier atoms (there are two barrier atoms between two adjacent atoms in the sequence for this direction; see **Table 2** for their position). The sequences are much shorter than along ⟨111⟩ (**Figure 3** and **4**) because a lot more energy is transferred to the neighbors of the atoms in the linear collision sequence. In fact, long energy transmission sequences can only take place along close packed directions, i.e. ⟨111⟩ and to a lesser extent ⟨100⟩ in bcc lattices. We can see that a lot of energy is transferred to the barrier atoms. When the collision is initiated along ⟨110⟩ or ⟨135⟩, or other lower-symmetry directions, two or three peaks at the most are observed. The impact of the short range interaction shows up readily in **Figure 6** that clearly shows that softer potentials (here CO21620 for Fe and MN-s for W) tend to transfer less energy to their barrier atoms (i.e. the peaks in red are less high) and the linear collision sequence is thus longer.

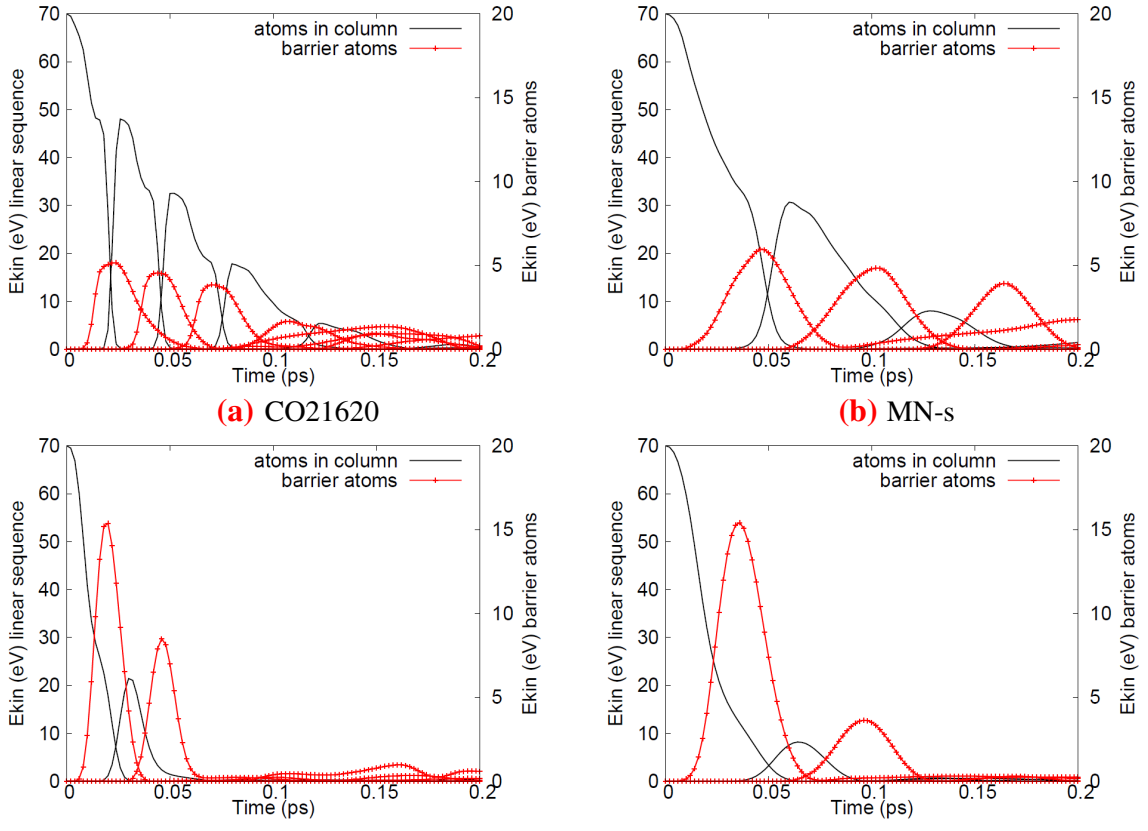

(a) CO21620 **(b)** MN-s

(c) MA10A **(d)** MN-h

Fe W

Figure 6: Comparison of the energy transfers during a linear collision sequence initiated by a 70 eV PKA along ⟨110⟩ for soft ((a) and (b)) and hard ((c) and (d)) potentials. The black curves correspond to the kinetic energy of the atoms in the linear collision sequence; the red curves to the kinetic energy of the side (or barrier) atoms.

The major difference between potentials is the amount of energy transferred, in the first collision, by the first head-on atom along ⟨110⟩ to the second head-on atom (compare the height of the first two black peaks) and to its barrier atoms (compare the height of the red peaks). Indeed, **Figure 7** shows that the remaining energy, which we refer to as the "energy dissipated in the lattice" (i.e. the energy which has neither been transferred to the head-on nor to its side atoms) is quite similar for all Fe potentials and all W potentials. In W, more energy is dissipated "to the lattice" than in Fe, and the RCS length is often shorter for ⟨110⟩ sequences in W than in Fe.

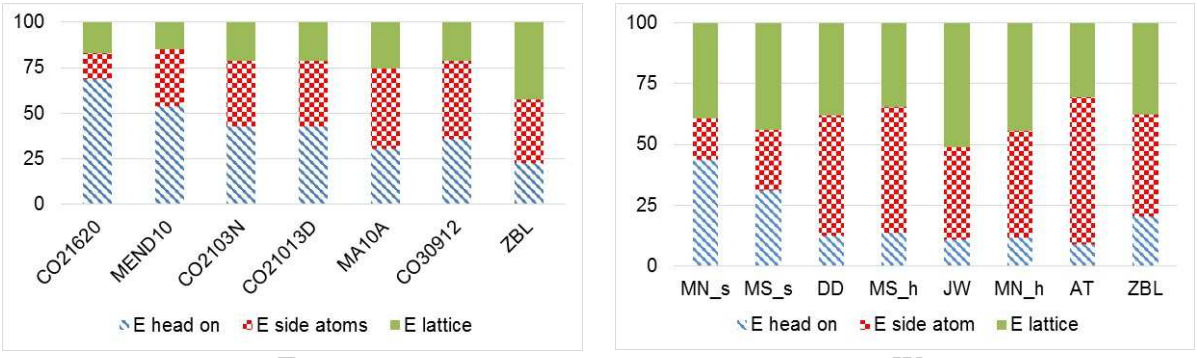

Fe W

Figure 7: Energy transferred to the first head-on atom (along ⟨110⟩), to its barrier atoms and to the "lattice" for a 70 eV RCS. The data are available in **Table TS1** of the supplementary material.

Linear collision sequence along ⟨111⟩

Figure 8 shows an example of the variation with time of the kinetic energy in linear collision sequences along ⟨111⟩ at 0 K for potentials in Fe and W. The black curves represent the kinetic

energy of the atoms in the sequence (as described in **section II.2**); the red curves represent the kinetic energy of the barrier atoms (there are two windows of three barrier atoms between two adjacent atoms in the sequence for this direction; see **Table 2** for their position). Compared to ⟨110⟩, little energy is transferred to barrier atoms and consequently the sequence is significantly longer. For example, there are more than 90 replacements in the 80 eV sequence in W. As the sequences are long the individual peaks cannot be differentiated, but the overall shapes speak for themselves. At some point, a transition is clearly seen in the way the energy is transmitted, significantly more energy is transmitted to barrier atoms similarly to what we observed for the ⟨110⟩ direction. In **Figure 8 a** and **b**, the initial linear collision energy was 80 eV, hardly any energy is transmitted to the neighbors (the red peaks are very small) and the decrease of the energy transmitted along the sequence (the height of the black peaks) is quite regular. In **Figure 8 c** and **d**, the initial linear collision energy was 90 eV, the energy transmitted to the barrier atoms starts increasing around 0.5 ps for the CO21620 potential and 0.55 ps for the MN-s potential (the red peaks increase). As a consequence, the energy transmitted to the atoms in the sequence (the black peaks) decreases much faster and the sequence ends.

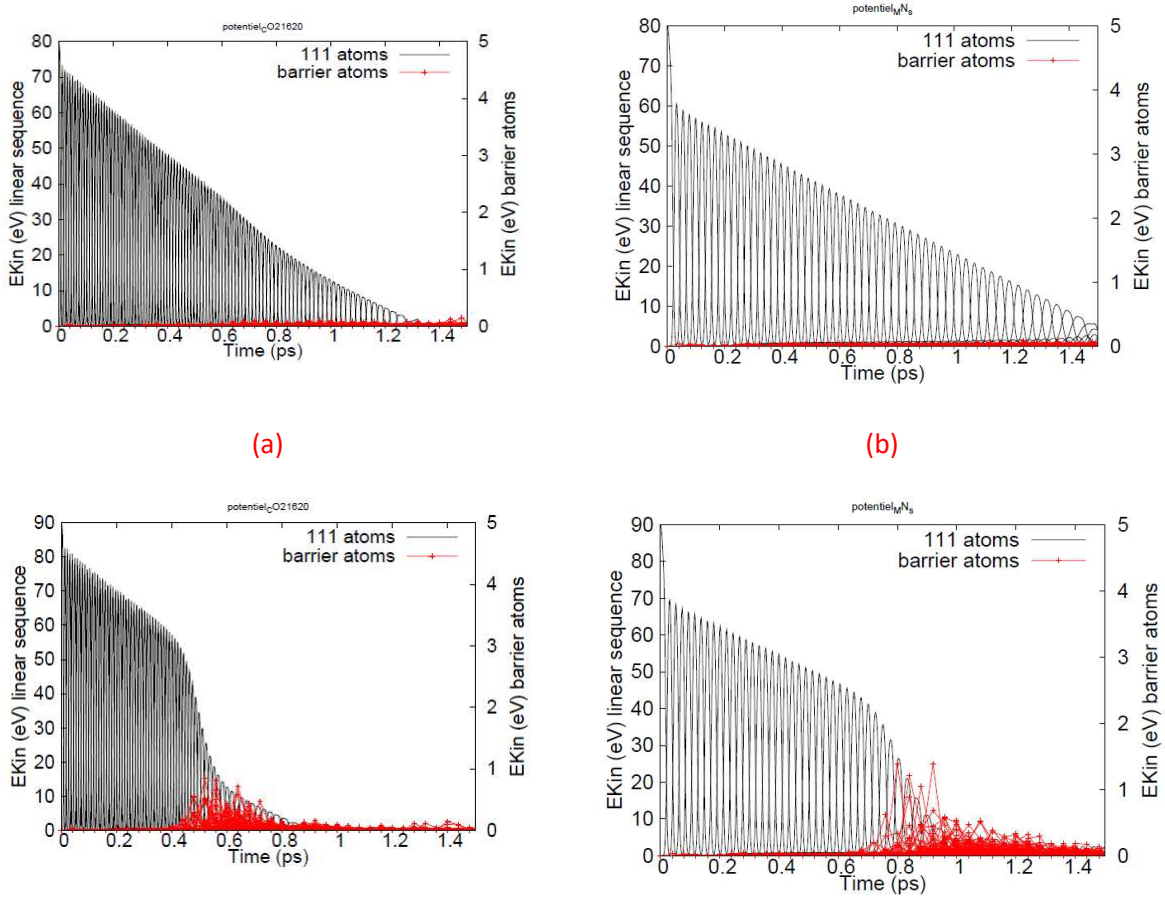

Figure 8: Illustration of the energy transfer regime changes in RCS. RCS along ⟨111⟩ for CO21620 and MN-s. The black curves correspond to the evolution of the individual kinetic energy of atoms along the sequence, the red curves to the evolution of the individual kinetic energy of the side atoms. As the sequences are long (there are more than 90 replacements in the 80 eV sequence in W (see **Figure 9**)), the individual peaks cannot be differentiated, but the overall shapes speak for themselves. (a) and (b): before the energy transfer change, i.e. the initial linear collision energy was 80 eV. (c) and (d): after the energy transfer change, i.e. the initial linear collision energy was 90 eV.

Figure 9 represents the evolution of the RCS length versus the initial collision energy for linear collision sequences along ⟨111⟩ for three W potentials. In these plots, an atom is considered to be displaced (and thus has created a replacement) when its displacement is larger than 90 % of the nearest neighbor distance ($\frac{\sqrt{3}}{2} l.u.$). The RCS length is the distance between the vacancy created by the ejection of the PKA from its lattice site and the crowdion created at the end of the sequence. Each curve displays three regions: the first one where no permanent displacement is made (the RCS length is zero); the second one where the RCS length increases with the sequence energy, i.e. the energy given to the PKA atom and the third one where the RCS length decreases when the sequence energy increases. The thresholds between the three regions depend strongly on the potentials. The threshold energy between the first two regions is the energy at which a first replacement takes place. It will be referred to as the replacement energy

threshold. The threshold between the last two regimes corresponds to a change in the energy transfer: the RCS length starts to decrease when the barrier atoms start taking in much more kinetic energy (**Figure 8)**. Because of the change in the energy transfer regime, the length of replacement collision sequences (RCS) in dense ⟨111⟩ direction has a maximum value.

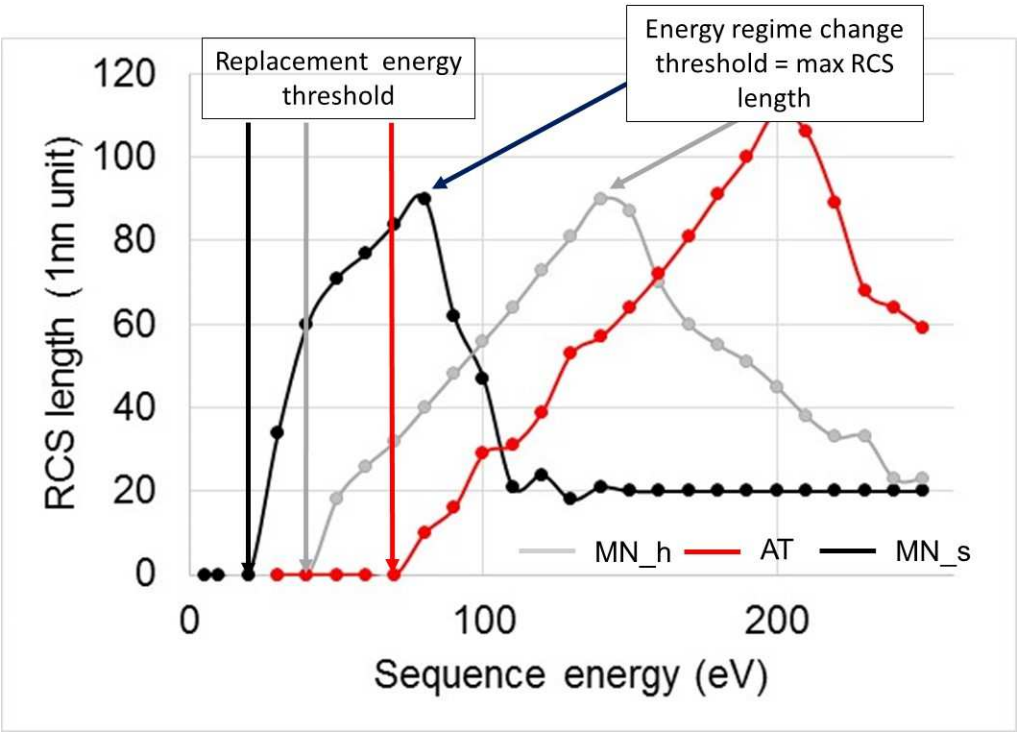

Figure 9: RCS length (in 1nn i.e. a√3/2 unit) versus linear collision energy for MN-h, MN_s and AT.

Table 3 presents all the energy thresholds for both materials investigated in this work. For the W potentials, the energy at which the RCS length starts to decrease is much lower for the soft potentials, than for the other potentials, whereas, for the Fe potentials, the differences are less significant. In W, **Figure 9** also shows that the soft potential creates more replacements than the harder ones at low linear collision energy, i.e. before the energy transfer change (compare the black curve to the grey curve in **Figure 9**). As a consequence, the maximum linear collision lengths are not so different between hard and soft potentials, and in fact for MN-h and MN-s they are identical, despite not being created at the same initial collision energy. For MS-h, note that the vacancy initiated at the beginning of the sequence, travels quite far along the sequence. Furthermore, a second RCS starts inside the first one above 190 eV.

Table 3: Energy regime change thresholds (eV) at which the energy transmission regime along ⟨111⟩ changes, for all the potentials investigated in this work.

	Threshold energy for replacement (eV)	Energy regime change threshold (eV)	Max linear collision length (nn distance)
	Fe potentials		
CO21620	30	70	92
CO30912	40	80	111
CO21013D	30	80	120
CO21013N	30	80	113
MEND10	90	100	102
MA10A	60	100	89
ZBL	50	120	95
	W potentials		
AT	80	210	113
MN-h	50	150	92
MN-s	30	80	92
MS-s	50	70	73
MS-h	50	240	100
JW	50	190	126
DD	40	160	101
ZBL	50	140	96

The well-known Fe potential MEND10 exhibits a peculiar behavior. Permanent displacements are only created at quite high PKA energy compared to the other Fe potentials. Indeed for PKA energies lower than 100 eV, very long sequences are initiated, as shown on **Figure S1** of the supplementary material, where 97 peaks are seen between 0 and 1.3 ps. The kinetic energy is thus transferred very far away from the PKA, however, the sequence reverses at some point and all the atoms move back to their original lattice site as none of them have passed through the second window and the overall number of replaced atoms is zero. One needs to give an impulse of at least 100 eV to create permanent replacements.

Note also that for the DD potential for W the energy transmission is not smooth at all as can be clearly seen (**Figure S2** in the supplementary).

3) Threshold displacement energies

Table 4 and **Figure 10** present the average TDEs obtained for all potentials. The distributions can be found **Figures S3** and **S4** of the supplementary material. We refer to the difference between the maximum and the minimum values obtained in the 200 simulations as the "distribution width". Comparison with other data found in the literature is not straightforward as the authors of [4], [12] and [30] used the approach proposed in [31]. This later approach was chosen to be more appropriate to compare with experimental data, i.e. by changing the angle between the direction under investigation and the momentum given to the initial atom. Furthermore, the TDE value they obtained is the minimum value of all the trials for a given direction, whereas in our case, we take the average of the minimum value we obtained for each

simulation. Because of the large dispersion of the data along the ⟨110⟩ and ⟨135⟩ directions, our results are thus very far from those of [4], [12] and [30].

The first obvious result from our data is that the TDEs are smaller for Fe than for W. Note that, for this property also, much larger variability in the mean TDEs is observed with the W potentials than with the Fe potentials. Furthermore, the TDE are the largest for the ⟨110⟩ and ⟨135⟩ directions, as could be expected from the fact that atoms moving along these directions come quite close to their barrier atoms (see **Table 2**).

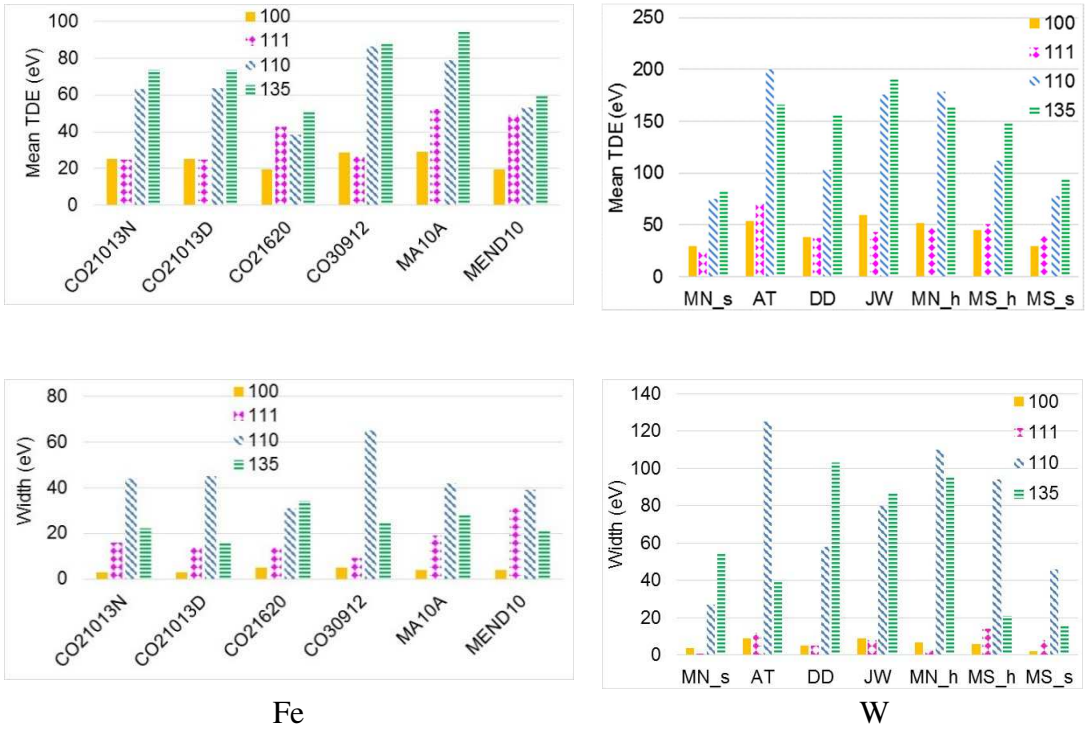

Figure 10: Mean TDEs (top) and distribution width (bottom) for W (left) and Fe (right) for the four directions investigated. **Figures S3** and **S4** in the supplementary material show the TDE's distributions for all W and Fe potentials.

Table 4: Average threshold displacement energies (eV) and standard deviations for all the potentials. The second line indicates, for each potential, the minimum energy of all 200 simulations, for a better comparison with other groups.

	⟨100⟩	⟨110⟩	⟨111⟩	⟨135⟩
W				
AT: this work	53 ± 1	200 ± 18	71 ± 2	166 ± 8
	51	105	68	150
AT at 36 K [4]*	57 ± 1	103 ± 1	89 ± 1	
DD: this work	38 ± 1	103 ± 11	37 ± 1	155 ± 25
	36	75	35	101
DD at 36 K [12]	41 ± 1	93 ± 1	41 ± 1	
JW: this work	59 ± 1	176 ± 25	43 ± 1	192 ± 11
	56	127	41	125
JW at 36 K [4]	63 ± 1	93 ± 1	61 ± 1	
MN-h: this work	51 ± 1	179 ± 17	48 ± 1	165 ± 23
	49	90	46	120
MN-s: this work	29 ± 1	75 ± 6	24 ± 1	82 ± 7
	28	60	24	60
MS-h: this work	45 ± 1	111 ± 15	51 ± 3	150 ± 3
	43	70	45	143
MS-h at 36 K [4]	43 ± 1	71 ± 1	65 ± 1	
MS-s: this work	30 ± 1	78 ± 5	40 ± 1	94 ± 3
	29	50	39	83
MS-s at 36 K [4]	31 ± 1	51 ± 1	45 ± 1	
DFT_{sd}: this work	40	63	44	103
DFT_{spd}: this work	58	81	>85	109
Exp. [34]	42 ± 2	>70	44 ± 1	
Fe				
CO21013: this work	25 ± 1	63 ± 12	25 ± 3	74 ± 4
	23	45	21	60
CO21013D: this work	25 ± 1	64 ± 13	25 ± 3	73 ± 3
	23	45	21	65
CO21620: this work	19 ± 1	38 ± 5	42 ± 3	51 ± 6
	17	20	36	30
CO30912: this work	29 ± 1	86 ± 16	27 ± 2	88 ± 4
	26	60	24	74
MA10A: this work	29 ± 1	79 ± 6	52 ± 4	94 ± 6
	27	55	43	74
MEND10: this work	20 ± 1	53 ± 8	49 ± 5	59 ± 5
	18	30	33	45
MEND10 at 0 K [5]	17 [5]	33 [5]	33[5]	55 [5]
MEND10 at 36 K [30]	19 ± 0.5 [30]	46 ± 2.4 [30]	42.6 ± 2.2 [30]	
	18.5 ± 0.2 [30]	46.5 ± 1.0 [30]	42.0 ± 0.8 [30]	
DFT_{sd} [5]	17	32	15	48
DFT_{psd} [5]	21	43	20	49
Exp. [35]	17	30-35	20	-
Exp. [36]	20	30		

* the uncertainties provided in references [4] [12] are ±1 eV because the thresholds were determined with an energy step size of 2 eV, see [31]; where as in [30] the uncertainties are standard errors of the means.

If we take as reference the TDE values obtained by DFT_{psd}, we find that for Fe, potential CO21620 is the best except along the ⟨111⟩ direction, whereas for W, the soft version of the MS potential is the closest, however it is "too soft" along the ⟨100⟩ direction. Note that for W, the TDE along the ⟨111⟩ direction obtained with DFT_{psd} is not yet fully determined because of the lack of energy barriers along that direction which makes displacement along ⟨111⟩ column very easy and requires thus prohibitively large boxes.

Figure 11 shows a clear correlation between TDEs along the ⟨110⟩ direction and TDEs along the 3 other directions for the two bcc metals explored in this work. This could be expected as a hard potential would probably be hard in all directions.

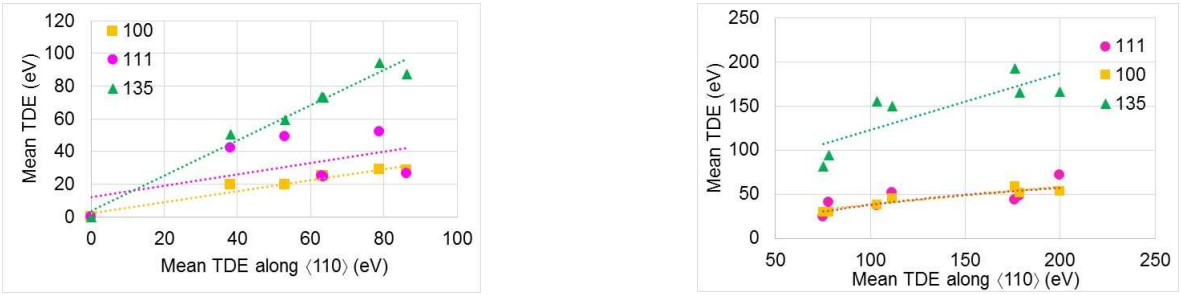

Fe W

Figure 11: Correlation between TDEs for all the potentials.

IV Discussion

Figure 12 shows the TDE distributions obtained along the ⟨110⟩ direction (Fig.12 (a) and (b)), the potential energy evolution during a QSD simulation (Fig.12 (c) and (d)), the evolution of the total energy of the initial atom in the sequence (first peak), first head-on atom (second peak) and second head-on atom (third peak) during a linear collision sequence along the same direction (Fig.12 (e) and (f)). We find that, along this direction, for both materials, correlations exist between the three properties and the primary damage. The potentials with the lowest TDEs in the ⟨110⟩ direction are the ones with the lowest QSD, and the ones that transmit the most energy from the PKA to the first head-on atom in the direction of the RCS sequence. These softer potentials also tend to transfer less energy to their side atoms as discussed in **section III-3 (Figure 6**) and previously shown [4].

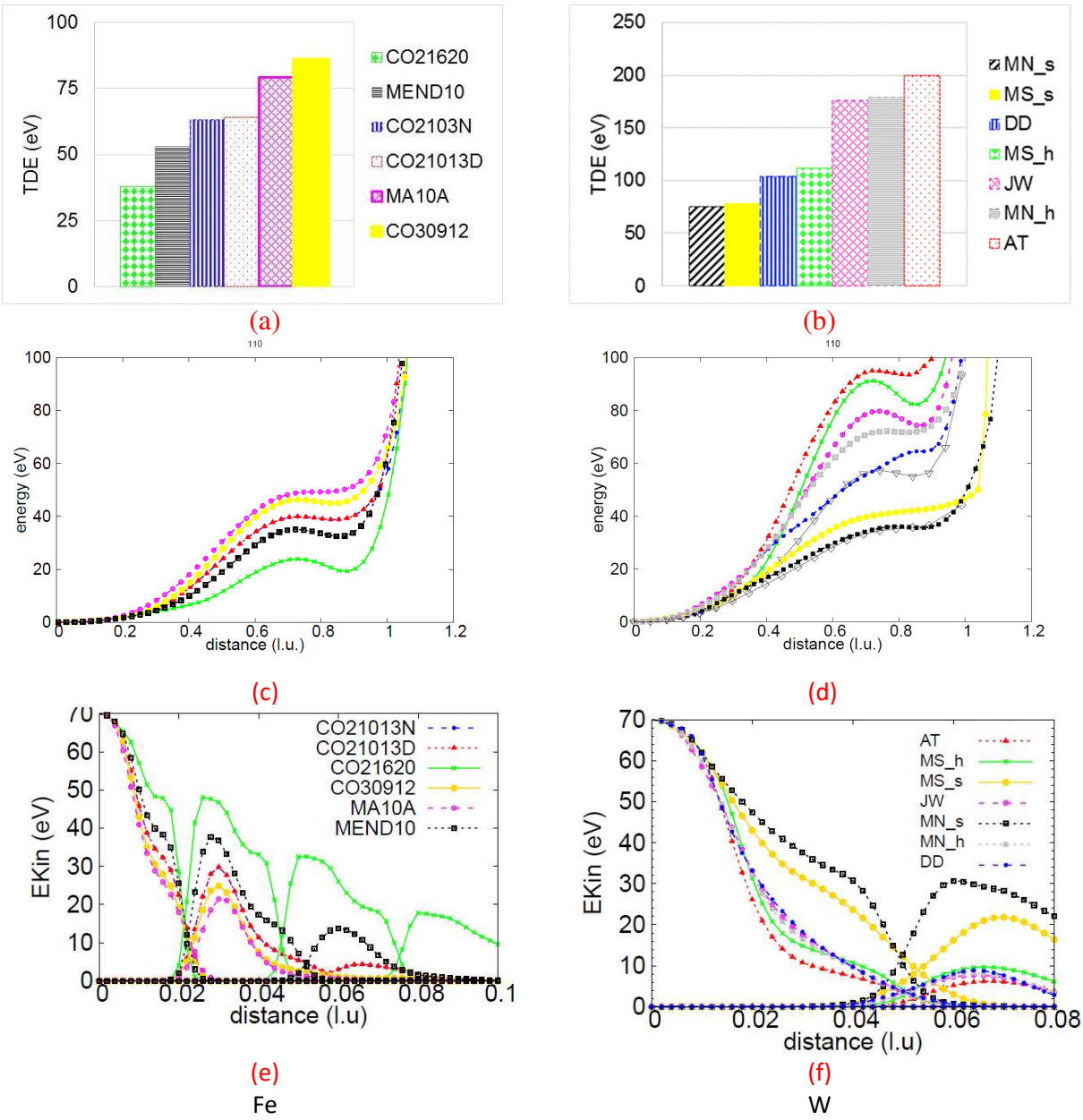

Figure 12: Mean TDE along ⟨110⟩ ((a),(b)); the QSD along ⟨110⟩ ((c),(d)); 70 eV linear collision sequence along ⟨110⟩ ((e),(f)). Left hand side: Fe, right hand side: W

A plot of the fraction of energy lost between the first atom in the ⟨110⟩ sequence and the first head-on atom, versus the height of the QSD bump shows a direct correlation **(Figure 12 (a))**. It can be reminded that the QSD bump height is the maximum potential energy when the drag atom passes close to its barrier / neighbor atoms (which corresponds to the interaction of the drag atom with the barrier atoms). This proves, not surprisingly, that the interaction with these atoms is very important and must be correctly accounted for the hardening of the potential. The correlation between the percentage of energy lost between the first atom in the ⟨110⟩ sequence and the first head-on atom, and the mean TDE for this direction is also quite clear **(Figure 12 (b)**). For the other directions, the trends are less obvious.

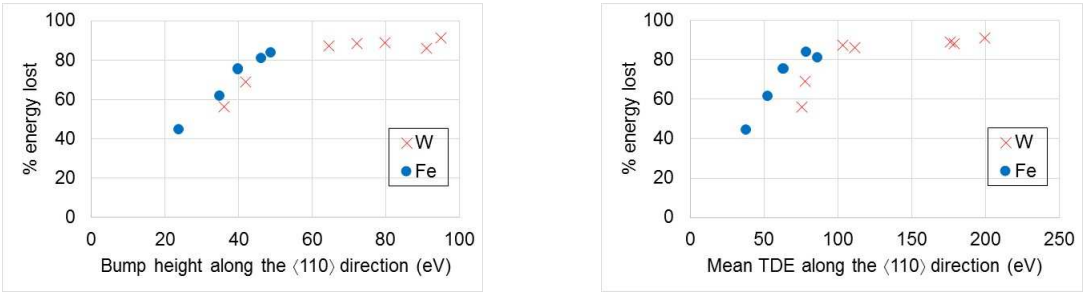

(a) (b)

Figure 13: Fraction of energy lost between a70 eV PKA and the first head on atom along ⟨110⟩ versus (a) the height of the bump in the QSD (left); the mean TDE along ⟨110⟩ (right).

Our results show that potential properties along the ⟨110⟩ direction are related. QSD along the ⟨110⟩ direction in bcc metals allows to probe interaction distances in region where the contribution of neighbors in the strength of the interaction between a moving atom and the one right in front of it. It is thus a good transition between the purely "pair" interaction of the ZBL and the many-body interaction of the equilibrium part of the potential. The heights of the bump at 0.707 l.u. is a direct measure of this interaction and it is quite easy to check whether the hardening procedure will reproduce it correctly or not. For this reason, we suggest that the DFT_{psd} results along that direction should be used to harden potentials derived for bcc metals. For other metals, the most appropriate direction will be likely to change depending on crystallographic considerations.

The primary damage created by all these potentials will be presented and analyzed in the companion paper, however we can add here that our data show that soft potentials predict more defects, as previously observed [4] but also more subcascades.

Conclusions

We have characterized a large panel of potentials for W and Fe, differing either by their equilibrium part or the way they were hardened. For these we determined for four directions: ⟨100⟩, ⟨110⟩, ⟨111⟩ and ⟨135⟩, their mean threshold displacement energies, replacement collision sequences (RCS) and quasi static drag (QSD) curves. Clear correlations were found between TDE, QSD and RCS along the ⟨110⟩ direction. Along this direction, the lower the TDE, the lower the QSD and the more energy is transmitted along the ⟨110⟩ direction during the RCS (i.e. the higher the secondary head-on atom peak height). For the ⟨100⟩ and ⟨135⟩ directions, the lower the TDEs the lower the QSD. For RCS along ⟨111⟩, a change in the energy transmission regime is observed when the PKA energy is increased. This change corresponds to more kinetic energy being transmitted to the side atoms. For the soft potentials, this change appears at lower energies than for the other potentials.
The major outcome of this work is thus that we recommend that in bcc metals, during the hardening procedure, care should be taken to reproduce correctly the interactions among atoms

moving along the ⟨110⟩ direction. Fitting the QSD along that direction is a convenient way to accomplish this and we will present the method in a forthcoming study.
We will show in the companion paper [7] that one consequence on the primary damage, based on large statistics for 80 keV cascades in Fe and 50 keV cascades in W for all potentials, is that soft potentials produce more subcascades, and those subcascades are also larger.

Acknowledgements

The authors wish to thank R. E. Stoller for the numerous discussions we had regarding this work which contributed to improve a great deal the manuscript. We acknowledge GENCI resources for part of the calculations (project DeFeT A0050910624). This work has been carried out within the framework of the EUROfusion Consortium and has received funding from the Euratom research and training programme 2014-2018 and 2019-2020 under grant agreement No 633053. The views and opinions expressed herein do not necessarily reflect those of the European Commission. This work was also partly supported within the European project SOTERIA (661913 and contributes to the Joint Programme on Nuclear Materials (JPNM) of the European Energy Research Alliance (EERA). The project leading to this publication has received funding from Excellence Initiative of Aix-Marseille University - A*MIDEX, a French Investissements d'Avenir programme as well as from the French National Research Agency (Grant No. ANR-18-CE05-0012).

Data availibility

The raw/processed data required to reproduce these findings cannot be shared at this time due to technical or time limitations but are available upon request.

References

[1] J.F. Ziegler, J.P. Biersack, The Stopping and Range of Ions in Matter, in: D.A. Bromley (Ed.), Treatise Heavy-Ion Sci., Springer US, Boston, MA, 1985: pp. 93–129. https://doi.org/10.1007/978-1-4615-8103-1_3.
[2] C.S. Becquart, C. Domain, A. Legris, J.C. Van Duysen, Influence of the interatomic potentials on molecular dynamics simulations of displacement cascades, J. Nucl. Mater. 280 (2000) 73–85. https://doi.org/10.1016/S0022-3115(00)00029-5.
[3] C.S. Becquart, A. Souidi, M. Hou, Relation between the interaction potential, replacement collision sequences, and collision cascade expansion in iron, Phys. Rev. B. 66 (2002). https://doi.org/10.1103/PhysRevB.66.134104.
[4] A.E. Sand, J. Dequeker, C.S. Becquart, C. Domain, K. Nordlund, Non-equilibrium properties of interatomic potentials in cascade simulations in tungsten, J. Nucl. Mater. 470 (2016) 119–127. https://doi.org/10.1016/j.jnucmat.2015.12.012.
[5] P. Olsson, C.S. Becquart, C. Domain, *Ab initio* threshold displacement energies in iron, Mater. Res. Lett. 4 (2016) 219–225. https://doi.org/10.1080/21663831.2016.1181680.
[6] R.E. Stoller, A. Tamm, L.K. Béland, G.D. Samolyuk, G.M. Stocks, A. Caro, L.V. Slipchenko, Yu.N. Osetsky, A. Aabloo, M. Klintenberg, Y. Wang, Impact of Short-Range

Forces on Defect Production from High-Energy Collisions, J. Chem. Theory Comput. 12 (2016) 2871–2879. https://doi.org/10.1021/acs.jctc.5b01194.
[7] A. De Backer, C.S. Becquart, P. Olsson, C. Domain, Modelling the primary damage in Fe and W: influence of the short range interactions on the cascade properties: part 2 – displacement cascades, (submitted).
[8] M.W. Finnis, J.E. Sinclair, A simple empirical *N* -body potential for transition metals, Philos. Mag. A. 50 (1984) 45–55. https://doi.org/10.1080/01418618408244210.
[9] D.R. Mason, D. Nguyen-Manh, C.S. Becquart, An empirical potential for simulating vacancy clusters in tungsten, J. Phys. Condens. Matter. 29 (2017). https://doi.org/10.1088/1361-648X/aa9776.
[10] N. Juslin, B.D. Wirth, Interatomic potentials for simulation of He bubble formation in W, J. Nucl. Mater. 432 (2013) 61–66. https://doi.org/10.1016/j.jnucmat.2012.07.023.
[11] P.M. Derlet, D. Nguyen-Manh, S.L. Dudarev, Multiscale modeling of crowdion and vacancy defects in body-centered-cubic transition metals, Phys. Rev. B. 76 (2007). https://doi.org/10.1103/PhysRevB.76.054107.
[12] C. Björkas, K. Nordlund, S. Dudarev, Modelling radiation effects using the ab-initio based tungsten and vanadium potentials, Nucl. Instrum. Methods Phys. Res. Sect. B Beam Interact. Mater. At. 267 (2009) 3204–3208. https://doi.org/10.1016/j.nimb.2009.06.123.
[13] G.J. Ackland, R. Thetford, An improved N-body semi-empirical model for body-centred cubic transition metals, Philos. Mag. A. 56 (1987) 15–30. https://doi.org/10.1080/01418618708204464.
[14] Y. Zhong, K. Nordlund, M. Ghaly, R.S. Averback, Defect production in tungsten: A comparison between field-ion microscopy and molecular-dynamics simulations, Phys. Rev. B. 58 (1998) 2361–2364. https://doi.org/10.1103/PhysRevB.58.2361.
[15] M.-C. Marinica, L. Ventelon, M.R. Gilbert, L. Proville, S.L. Dudarev, J. Marian, G. Bencteux, F. Willaime, Interatomic potentials for modelling radiation defects and dislocations in tungsten, J. Phys. Condens. Matter. 25 (2013) 395502. https://doi.org/10.1088/0953-8984/25/39/395502.
[16] L. Malerba, M.C. Marinica, N. Anento, C. Björkas, H. Nguyen, C. Domain, F. Djurabekova, P. Olsson, K. Nordlund, A. Serra, D. Terentyev, F. Willaime, C.S. Becquart, Comparison of empirical interatomic potentials for iron applied to radiation damage studies, J. Nucl. Mater. 406 (2010) 19–38. https://doi.org/10.1016/j.jnucmat.2010.05.017.
[17] G.J. Ackland, M.I. Mendelev, D.J. Srolovitz, S. Han, A.V. Barashev, Development of an interatomic potential for phosphorus impurities in -iron, J. Phys. Condens. Matter. 16 (2004) S2629–S2642. https://doi.org/10.1088/0953-8984/16/27/003.
[18] R. Alexander, M.-C. Marinica, L. Proville, Interatomic potentials for irradiation-induced defects in iron, Phys. Rev. B. 94 (2016).
[19] G. Kresse, J. Hafner, *Ab initio* molecular dynamics for liquid metals, Phys. Rev. B. 47 (1993) 558–561. https://doi.org/10.1103/PhysRevB.47.558.
[20] G. Kresse, J. Furthmüller, Efficient iterative schemes for *ab initio* total-energy calculations using a plane-wave basis set, Phys. Rev. B. 54 (1996) 11169–11186. https://doi.org/10.1103/PhysRevB.54.11169.
[21] P.E. Blöchl, Projector augmented-wave method, Phys. Rev. B. 50 (1994) 17953.
[22] G. Kresse, D. Joubert, From ultrasoft pseudopotentials to the projector augmented-wave method, Phys. Rev. B. 59 (1999) 1758.
[23] J.P. Perdew, J.A. Chevary, S.H. Vosko, K.A. Jackson, M.R. Pederson, D.J. Singh, C. Fiolhais, Atoms, molecules, solids, and surfaces: Applications of the generalized gradient approximation for exchange and correlation, Phys. Rev. B. 46 (1992) 6671.

[24] L. Wilk, M. Nusair, S.H. Vosko, The Fermi contact contribution to the Knight shift in Be from self-consistent spin-polarized calculations, Can. J. Phys. 59 (1981) 585–595. https://doi.org/10.1139/p81-076.
[25] H.J. Monkhorst, J.D. Pack, Special points for Brillouin-zone integrations, Phys. Rev. B. 13 (1976) 5188–5192. https://doi.org/10.1103/PhysRevB.13.5188.
[26] C.S. Becquart, A. Souidi, M. Hou, Replacement collision and focuson sequences revisited by full molecular dynamics and its binary collision approximation, Philos. Mag. 85 (2005) 409–415. https://doi.org/10.1080/02678370412331320251.
[27] R.E. Stoller, G.R. Odette, B.D. Wirth, Primary damage formation in bcc iron, J. Nucl. Mater. 251 (1997) 49–60. https://doi.org/10.1016/S0022-3115(97)00256-0.
[28] M.J. Norgett, M.T. Robinson, I.M. Torrens, A proposed method of calculating displacement dose rates, Nucl. Eng. Des. 33 (1975) 50–54. https://doi.org/10.1016/0029-5493(75)90035-7.
[29] L. Malerba, Molecular dynamics simulation of displacement cascades in α-Fe: A critical review, J. Nucl. Mater. 351 (2006) 28–38. https://doi.org/10.1016/j.jnucmat.2006.02.023.
[30] J. Byggmästar, F. Granberg, K. Nordlund, Effects of the short-range repulsive potential on cascade damage in iron, J. Nucl. Mater. 508 (2018) 530–539. https://doi.org/10.1016/j.jnucmat.2018.06.005.
[31] K. Nordlund, J. Wallenius, L. Malerba, Molecular dynamics simulations of threshold displacement energies in Fe, Nucl. Instrum. Methods Phys. Res. Sect. B Beam Interact. Mater. At. 246 (2006) 322–332. https://doi.org/10.1016/j.nimb.2006.01.003.
[32] W. Setyawan, A.P. Selby, N. Juslin, R.E. Stoller, B.D. Wirth, R.J. Kurtz, Cascade morphology transition in bcc metals, J. Phys. Condens. Matter. 27 (2015) 225402. https://doi.org/10.1088/0953-8984/27/22/225402.
[33] C.S. Becquart, K.M. Decker, C. Domain, J. Ruste, Y. Souffez, J.C. Turbatte, J.C. Van Duysen, Massively parallel molecular dynamics simulations with EAM potentials, Radiat. Eff. Defects Solids. 142 (1997) 9–21. https://doi.org/10.1080/10420159708211592.
[34] F. Maury, M. Biget, P. Vajda, Frenkel pair creation and stage I recovery in W crystals irradiated near threshold, Radiat. Eff. 38 (1978) 53–65.
[35] F. Maury, M. Biget, P. Vajda, A. Lucasson, P. Lucasson, Anisotropy of defect creation in electron-irradiated iron crystals, Phys. Rev. B. 14 (1976) 5303–5313. https://doi.org/10.1103/PhysRevB.14.5303.
[36] J.N. Lomer, M. Pepper, Anisotropy of defect production in electron irradiated iron, Philos. Mag. 16 (1967) 1119–1128. https://doi.org/10.1080/14786436708229961.